Armor for Steel: Facile Synthesis of Hexagonal Boron Nitride Films on Various Substrates

Ivan Vlassiouk, Sergei Smirnov, Alexander Puretzky, Olugbenga Olunloyo, David B. Geohegan, Ondrej Dyck, Andrew R. Lupini, Raymond R. Unocic, Harry M. Meyer III, Kai Xiao, Dayrl Briggs, Nickolay Lavrik, Jong Keum, Ercan Cakmak, Sumner B. Harris, Marti Checa, Liam Collins, John Lasseter, Reece Emery, John Rayle, Philip D. Rack, Yijing Stehle, Pavan Chaturvedi, Piran R. Kidambi, Gong Gu, and Ilia Ivanov*

While hexagonal boron nitride (hBN) has been widely used as a buffer or encapsulation layer for emerging electronic devices, interest in utilizing it for large-area chemical barrier coating has somewhat faded. A chemical vapor deposition process is reported here for the conformal growth of hBN on large surfaces of various alloys and steels, regardless of their complex shapes. In contrast to the previously reported very limited protection by hBN against corrosion and oxidation, protection of steels against 10% HCl and oxidation resistance at 850 °C in air is demonstrated. Furthermore, an order of magnitude reduction in the friction coefficient of the hBN coated steels is shown. The growth mechanism is revealed in experiments on thin metal films, where the tunable growth of single-crystal hBN with a selected number of layers is demonstrated. The key distinction of the process is the use of N_2 gas, which gets activated exclusively on the catalyst's surface and eliminates adverse gas-phase reactions. This rate-limiting step allowed independent control of activated nitrogen along with boron coming from a solid source (like elemental boron). Using abundant and benign precursors, this approach can be readily adopted for large-scale hBN synthesis in applications where cost, production volume, and process safety are essential.

1. Introduction

Hexagonal boron nitride (hBN) has emerged as a foundational 2D material with a flat layered structure, chemical inertness, and a large thermal stability window similar to those of graphene, yet with an ultra-wide bandgap (≈6 eV). These attributes promise a large variety of applications. Besides utilization as a substrate, a gate dielectric, an interlayer or encapsulating insulator, and even an active material in electronic, photonic, and quantum devices,[1–4] a class of applications with broader relevance to industry involves hBN as a superior protective layer preventing corrosion, offering high-temperature oxidation resistance, inhibiting scale formation, reducing friction, etc.[5–9] Both application classes require high-quality hBN, but the latter must be employed on a very large scale and thus has

I. Vlassiouk, A. Puretzky, O. Olunloyo, D. B. Geohegan, O. Dyck, A. R. Lupini, R. R. Unocic, K. Xiao, D. Briggs, N. Lavrik, J. Keum, S. B. Harris, M. Checa, L. Collins, I. Ivanov
Center for Nanophase Materials Sciences
Oak Ridge National Laboratory
Oak Ridge, TN 37831, USA
E-mail: vlassioukiv@ornl.gov

S. Smirnov
Department of Chemistry and Biochemistry
New Mexico State University
Las Cruces, NM 88003, USA

S. Smirnov
NM Devices LLC
690 Canyon Point, Las Cruces, NM 88011, USA

J. Lasseter, R. Emery, J. Rayle, P. D. Rack
Department of Materials Science and Engineering
University of Tennessee
Knoxville, TN 37996, USA

Y. Stehle
Department of Mechanical Engineering
Union College
Schenectady, NY 12308, USA

P. Chaturvedi, P. R. Kidambi
Department of Chemical and Biomolecular Engineering
Vanderbilt University
Nashville, TN 37240, USA

The ORCID identification number(s) for the author(s) of this article can be found under https://doi.org/10.1002/admi.202300704

DOI: 10.1002/admi.202300704

significantly more stringent requirements for scalability, safety, and the process cost.

The "gold standard" approach for the highest quality hBN-based devices employs exfoliated flakes from bulk hBN single crystals synthesized by slow cooling of fluxes containing boron and nitrogen precursors, or boron nitride powder.[10–13] Such bulk crystal growth processes are long (>24 h) and requires high-temperature furnaces (>1500 °C). High temperature (>1250 °C) growth from FeB was also reported.[14] By comparison, chemical vapor deposition (CVD) can produce much larger hBN films and wafer-scale films are routinely reported.[15–17] So far, hBN produced by CVD typically have had inferior quality as compared to the exfoliated samples, even though specially engineered substrates allowed the growth of epitaxial single-crystal CVD hBN films.

Recently, large-scale single-crystal samples including mono- and few-layer hBN were grown on specially engineered Au, Cu, Ni, and NiFe substrates using borazine (liquid) or ammonia borane (solid) as a precursor.[18–22] Using these precursors is challenging not only due to safety and cost, but their decomposition is also difficult to control in a large reactor and the B:N ratio changes over the reactor length despite using a precursor with the initial 1:1 ratio. It complicates the growth process, especially in larger than lab-scale reactors,[23] enough to evoke usage machine learning for process optimization.[24] More convenient gaseous precursors, a mixture of diborane and ammonia, were also investigated, but the results were even less encouraging as uncontrollable deposition of various BN particles and polymers within the CVD reactor was observed.[25–28] These precursors are also toxic, which introduces safety issues into the logistics of scalable synthesis.

Here we present a facile and scalable method for atmospheric pressure CVD growth of hBN using gaseous molecular nitrogen and various forms of solid boron (B, B_2O_3, or B_4C) as the precursors, which are abundant, benign, and convenient – all the necessary traits for large-scale industrial production. Despite being counterintuitive, the chemical stability of the N_2 molecule is a key to the process control. We have identified nitrogen dissociative adsorption on a catalytic substrate surface as the rate-limiting step, reminiscent of the Haber-Bosch process.[29,30] It allows for control of activated N supply independently from the boron supply, which is self-limited from its minute amount of vapor. This eliminates undesirable gas-phase reactions, which have been a major concern in the standard hBN CVD synthesis with more reactive N feedstock. Through understanding the growth mechanism and after illustrating the resulting hBN film properties (**Figures 1–4**) in typical lab-scale experiments, we demonstrate (**Figures 5** and **6**) that such catalytic hBN growth can be extended to the industry relevant scale, limited only by the reactor size, allowing coating on various industrial metal items such as stainless steels 304 and 316, mild steels, cupronickels, and Inconel. We then showcase unprecedented performance of the hBN grown on widely used stainless steel 304, including protection against corrosion in 10% HCl for 10 days and against high-temperature oxidation in air at 850 °C for several hours. We anticipate that the demonstrated approach will be readily adopted for large-scale hBN synthesis for applications where cost, production volume, and process safety are essential. On the other hand, our investigation of the growth mechanism also reveals the potential of this approach for large-area, single-crystal hBN coatings on metal and metallic alloy thin films for use in emerging electronic and photonic devices. Nickel substrates yield mostly monolayers, while the addition of iron increases the number of hBN layers.

2. Results and Discussion

In previous experiments with hBN synthesis using borazane as a precursor we found that molecular nitrogen can be activated on the surface of the catalyst and reduce the negative effect of nitrogen loss in a long reactor.[23] Here we chose more efficient catalyst substrates and explore whether more benign sources of boron can be employed. Surprisingly, we initially noticed that when a solid elemental boron piece was placed upstream or suspended over Ni or/and Fe-containing metal foils or thin films, and then annealed in a N_2-containing atmosphere, hBN was formed on top of the substrate.

The growth process can be illustrated in a configuration where a cm-sized boron piece is placed on top of a quartz support positioned on top of the catalytic substrate, as shown in Figure 1a. The catalytic substrate here is a 500 nm-thick metal (Ni-Fe) film deposited on SiO_2/Si wafer. Upon heating, boron species are released, and their concentrations decline with distance from the boron piece, while the nitrogen concentration stays constant throughout the CVD reactor, as sketched in Figure 1b. hBN forms at the catalyst substrate close to the boron source, where the concentration of boron is sufficiently high, and does not form anywhere else, such as under the supporting quartz plate or far away from the boron chunk. SEM images show a distinct contrast between the hBN overlayer and the bare catalyst allowing unambiguous determination of the hBN region. In the example shown in Figure 1c the region for hBN growth extends only 2 mm away from the quartz edge. The hBN growth front is on the right side of the image extending away from the boron source and the hBN edge close to the quartz plate is abrupt with only rare hBN crystals not attached to the main growth region. Characteristic triangular hBN edges are also apparent in the vicinity of the quartz support edge as detailed in Figure S1 (Supporting Information). XPS confirms the assignment of the hBN formation region observed in the SEM image with the clear boron (≈190 eV) and nitrogen (≈398 eV) signals within hBN formation zone and the correspondingly negligible signals outside (see Figure 1c,d).

G. Gu
Department of Electrical Engineering and Computer Science
The University of Tennessee
Knoxville, TN 37996, USA
O. Olunloyo
Department of Physics and Astronomy, University of Tennessee
Knoxville 37996, United States
H. M. Meyer III
Chemical Sciences Division, Oak Ridge National Laboratory
Oak Ridge 37831, USA
E. Cakmak
Materials Science and Technology Division
Oak Ridge National Laboratory
Oak Ridge 37831, USA

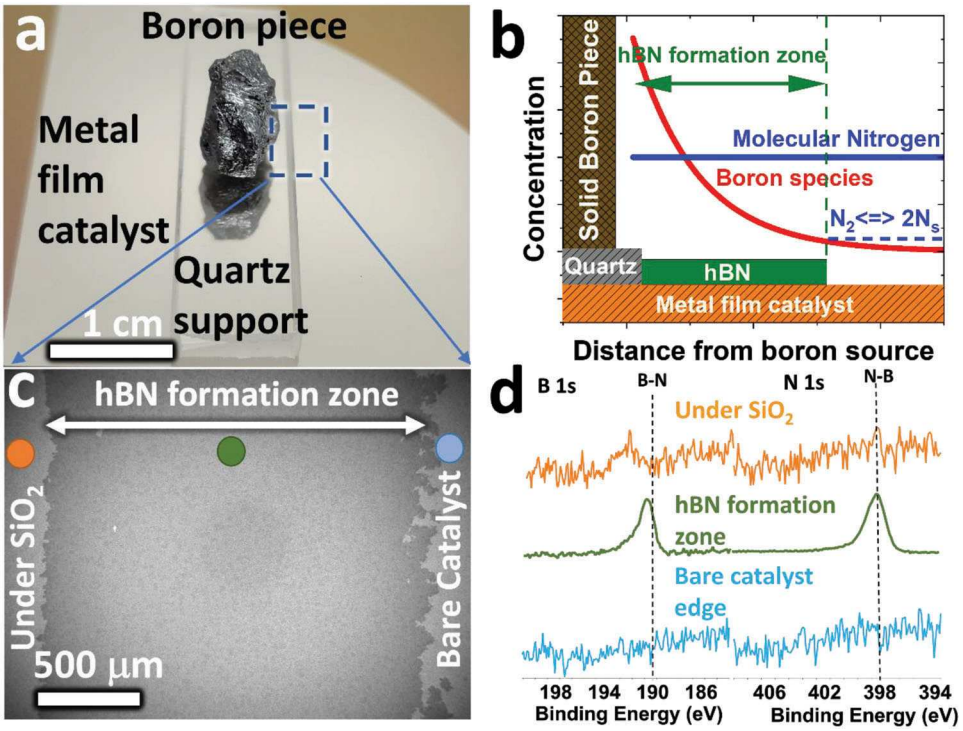

Figure 1. Growth of hBN from a boron piece and N_2 on a Ni/SiO_2 wafer. a) Photograph of the boron piece placed on the quartz support positioned on a Ni/SiO_2/Si wafer. b) Schematic of boron/nitrogen species concentration profiles. With the rate limiting step (catalyst + $N_2 \Leftrightarrow 2N_s$) highlighted c) SEM image of the hBN formation zone – darker contrast is hBN overlayer, bright regions on the left and right sides – bare catalyst. d) XPS spectra confirm the formation of hBN on the locations shown in (c).

2.1. Crucial Parameters Affecting the hBN Growth

With a basic growth process established, we can identify the most crucial experimental parameters affecting the growth. First, boron hydrides, B_xH_y, are known to be much more volatile than elemental boron and so we assess whether they might play a role. We find that the width of the hBN deposition zone does not depend on the hydrogen partial pressure, P_{H2}, between 0.3% and 10%, as shown in Figure 2a. At very high pressures (50%) the zone decreases due to reduction of the nitrogen partial pressure, P_{N2}, as confirmed in Figure 2b. The simplest explanation for the results would be that the formation of hydrides plays no role here. Indeed, even with zero hydrogen partial pressure, boron nitride is found on the catalyst surface by XPS almost with the same deposition width as with hydrogen (Figure S2, Supporting Information). Yet one must appreciate that supplying minute amounts of hydrogen in the experiments (typically 2.5%, unless specified otherwise) is needed to mitigate potential oxidation from trace amounts of oxygen. The latter can also contribute to the generation of volatile boron oxide species and thus facilitate boron transport to the catalytic substrate. The vapor pressure of pure boron, P_B, at 1100 °C is small (Section 2, Supporting Information) and we cannot unambiguously conclude that boron is transported to the catalytic substrate in the form of elemental boron vapor, its hydride or oxide. In any case, the amount of boron species in the gas phase is insignificant and, judging by the finite size of the hBN deposit, is consumed near the precursor.

Second, the width of the hBN deposition zone depends almost linearly on P_{N2}, as shown in Figure 2b, where dilution of nitrogen by argon allowed maintaining the same atmospheric pressure inside the reactor. Such a dependence suggests that dissociative adsorption of molecular nitrogen on the catalyst (catalyst + $N_2 \Leftrightarrow 2N_s$) is the rate-liming step, like in the Haber-Bosch process. Similarity to the process of industrial ammonia synthesis is apparent since similar catalysts are used in both processes.[29,30] The red point in Figure 2b corresponds to 50% nitrogen dilution by hydrogen, instead of argon as in the rest of the data (black points), but shows no apparent change in the growth outcome. Obviously, at zero nitrogen pressure hBN does not grow, however traces of boron can still be found on the catalyst surface by XPS. Thus, one can conclude that dissociative adsorption of molecular nitrogen on the catalyst is the rate-liming step.

Third, the temperature dependence is in line with the exothermic nature of hBN formation, $1/2N_2 + B \Leftrightarrow hBN + 254$ kJ/mol, resulting in larger yields at lower temperatures (Section 3, Supporting Information). Indeed, lowering the synthesis temperature from 1100 to 1000 °C, and further down to 900 °C, correspondingly widens the hBN formation zone from 5 mm to 8 mm and 13 mm, as shown in Figure 2c. Ammonia formation ($3H_2 + N_2 \Rightarrow 2NH_3 + 91.8$ kJ mol^{-1}) is also exothermic and this wider growth zone is consistent with the nitrogen activation being the rate-limiting step. In addition to a broader deposition zone, lowering the synthesis temperature results in smaller hBN crystals and an abundance of hBN crystals separated from the main hBN

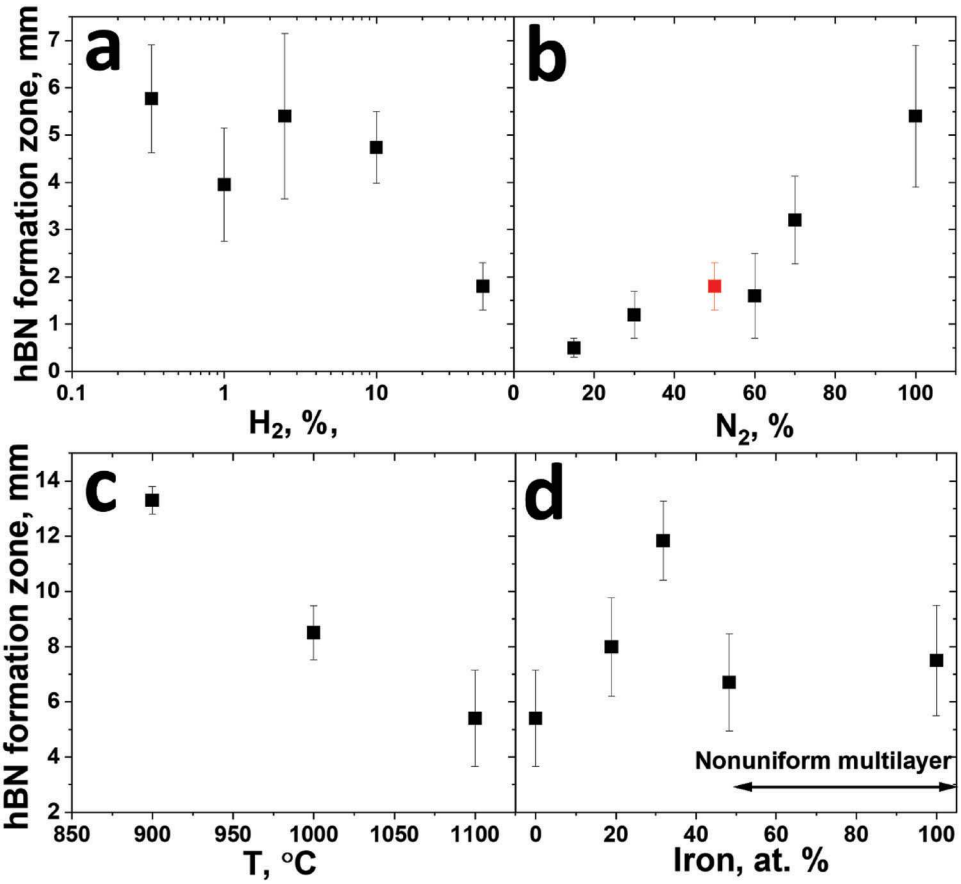

Figure 2. Dependence of hBN formation zone width on experimental parameters. a) Dependence on the hydrogen partial pressure (P_{H2}) b) versus nitrogen partial pressure (P_{N2}), where nitrogen was diluted with argon, except red point where dilution was done by hydrogen (same 50% dilution point is shown in (a)) c) versus synthesis temperature d) versus iron content in the catalytic substrate FeNi.

continuous deposition region that spreads over longer distance, as detailed in Figure S4 (Supporting Information). This obviously makes the quality of the resultant hBN poorer, with smaller monocrystalline domains and greater number of boundaries between them. Such boundaries are not only mechanically weak but also chemically inhomogeneous regions. Thus, despite the larger coverage, deposition at lower temperatures is not desirable.

Fourth, we consider the effect of catalyst composition. Iron is known to be a strong catalyst for nitrogen dissociative adsorption in the well-known Haber-Bosch process and we evaluate its effect on the growth of hBN by adding different amounts of Fe to the Ni catalyst. Adding iron to the nickel catalyst enhances the film growth area but also promotes multilayer hBN growth. Both features are consistent with N_2 activation being the rate-limiting step. The hBN formation zone widens with increasing the iron content in the catalyst up to 30%, but further increase results in a reduction of hBN growth region (see Figure 2d) and triggers nonuniform multilayer formation instead. This is likely due to a greater nitrogen dissolution in nickel-iron alloys compared to pure nickel.[31] The multilayer formation is likely similar to that of graphene on Ni, where multilayers are formed via precipitation of carbon dissolved in the catalyst material during cooling. The phase diagrams for nickel-boron[32] and iron-boron[33] are quite complex, which makes the interpretation not as obvious as with graphene, especially for FeNi alloys. Importantly, FeNi thin films have the same FCC (111) preferred orientation up to even 50% FeNi composition (Figure S5, Supporting Information). For pure iron films the preferred orientation is close to (100) and has a BCC crystal structure, which yields multilayer hBN films under the same growth conditions.

Atomic force microscopy (AFM) analysis in Figure 3a shows that the thickness increases from 2.3 ± 1.0 nm for hBN films grown on 25 at% iron in nickel (25FeNi) to 8.2 ± 3.0 nm for 40FeNi. It suggests that even at 25% Fe hBN is formed in multilayers and higher Fe content not only triggers increase of the hBN thickness, but also results in less uniform films. STEM images in Figure 3b show characteristic monolayer on pure nickel and ≈20 hBN layers on 40FeNi. Examples of the layer number analysis are shown in Figure S6 (Supporting Information). The depth profiles of boron and nitrogen obtained by Ar^+ etching in XPS also suggest thicker hBN films on Fe-containing catalysts confirming AFM data (see Figure 3c; Figure S3, Supporting Information). Additional characterization is shown in Section 4 (Supporting Information).

The Raman spectrum of hBN lacks an established sensitive metric for identifying defects, unlike in graphene, where the D/G Raman peaks ratio is commonly used for that purpose.[34–36] For hBN, many studies rely on the width of E_{2g} 1365 cm^{-1} Raman

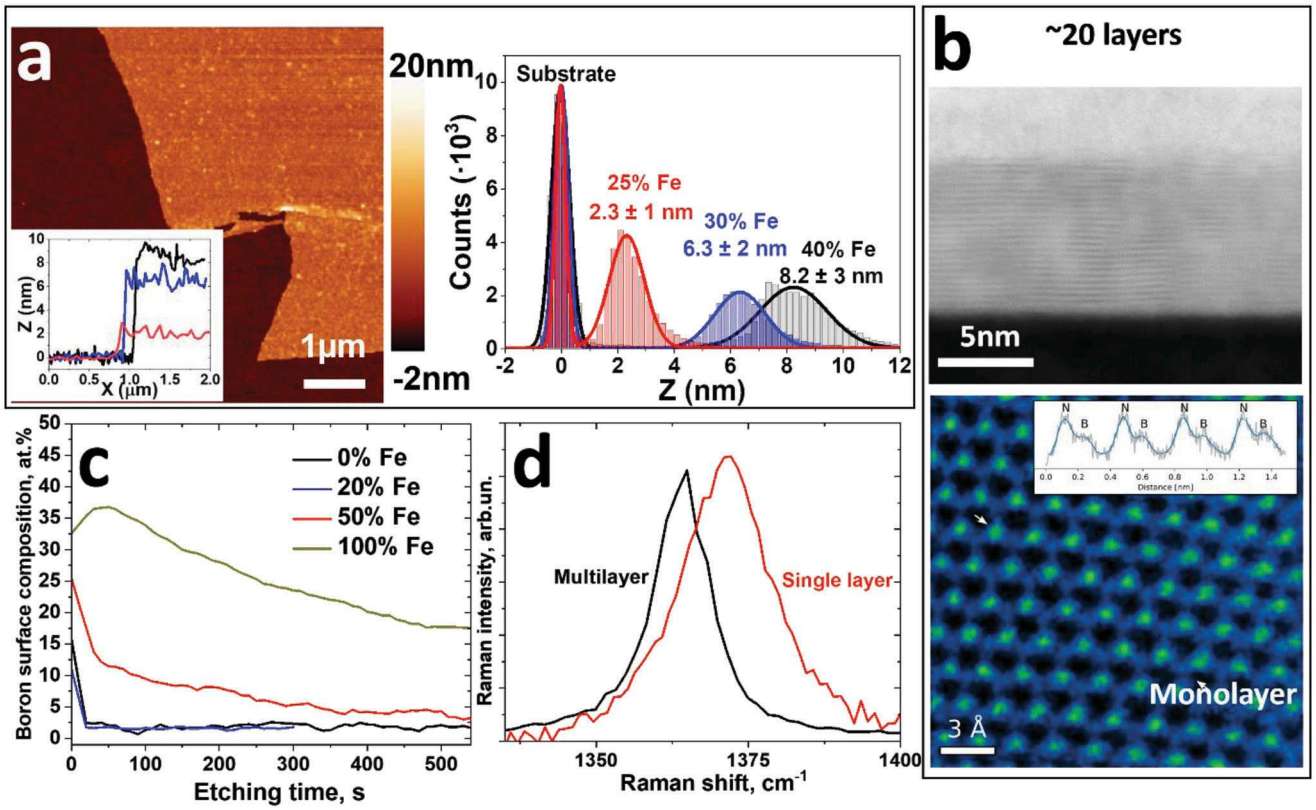

Figure 3. a) AFM image of hBN films grown on 30 at% iron in nickel (30FeNi) films and transferred onto SiO_2 (left). Insert shows height profiles of hBN grown on 25FeNi (red), 30FeNi (blue) and 40FeNi (black). hBN films thickness histograms with the same color legend (right). b) STEM image of hBN cross section (20 layers) grown on 40FeNi (top) and plane view monolayer hBN (bottom). Bright green spots are nitrogen, dim blue – boron atoms. Insert shows intensity profile along the line between two white arrows on the main image. c) Boron depth profile by XPS for films grown on catalyst with different Fe content. Note stronger boron signal for higher Fe content. d) Raman spectrum showing 11.5 cm^{-1} FWHM line at 1365 cm^{-1} for a multilayer hBN film grown on pure iron foils (black) and 18 cm^{-1} FWHM line at 1372 cm^{-1} for monolayer hBN grown on thin Ni film (red).

line as a quality metric.[13] The width and position of the E_{2g} peak depend on the number of hBN layers and thus a direct comparison of a monolayer with thicker samples is not universally applicable. For example, thicker hBN films grown on pure Fe have a red-shifted E_{2g} band compared to monolayer grown on Ni thin films (1365 vs. 1372.5 cm^{-1}) and narrower width (FWHM 11.5 vs. 18 cm^{-1}), as illustrated in Figure 3d.

2.2. Large Single-Crystal hBN

Most studies of CVD synthesis of hBN report its epitaxial growth on (111) catalyst surfaces,[4,22,37–39] and a similar outcome is observed here as well, but not always. An epitaxial growth regime is observed for hBN samples grown on 500 nm thick Ni(111) films prepared on Al_2O_3 (0001).[40] After 1 h growth at 1100 °C, centimeter-sized samples were transferred on a SiO_2/Si wafer for further investigation.

The epitaxial growth can be verified by mapping the angular dependence of the second harmonic generated (SHG) signal over an hBN sample.[22] Figure 4a illustrates it for our hBN grown on (111) Ni on sapphire. The SHG intensity, $I_{2\omega}$, is well fitted with the expected hBN single crystal dependence, $I_{2\omega} \sim \cos^2(3\phi+\phi_0)$, where ϕ is the laser polarization angle at the surface and ϕ_0 is the crystallographic orientation of the hBN sample.[41] An example of the SHG intensity polar plot as a function of excitation polarization angle is shown by the black points (experimental data) with a red fitted line. Individual $I_{2\omega}$ with 60-degree lobes observed on the hBN sample at different locations illustrate the single-crystal appearance at each point. Moreover, the same orientation angle ϕ_0 over the sample suggests that the hBN crystal extends over the whole sample length.

SEM images in Figure 4b of an incompletely grown monolayer (shorter times) reveal large, ≈500 μm, hBN individual crystals with trapezoidal shapes having identical orientation, in line with the single-crystal sample appearance from the SHG data. Similar truncated triangle-like hBN crystal shapes were also recently observed for epitaxial growth on Ni(111) foils, but they were much smaller.[22] More information on the observed crystal shapes is given in Section 3 (Supporting Information). When grown on polycrystalline Ni/SiO_2/Si substrate, hBN crystals are also not aligned but they can grow across the Ni grain boundaries from one Ni domain to the neighboring ones without recognizable shape change – see triangular crystals in Figure S1 (Supporting Information). This suggests that *nonepitaxial* growth dictated by the hBN crystal edge can also occur, at least for some synthesis conditions, which implies the possibility of realizing single crystal growth of hBN on polycrystalline

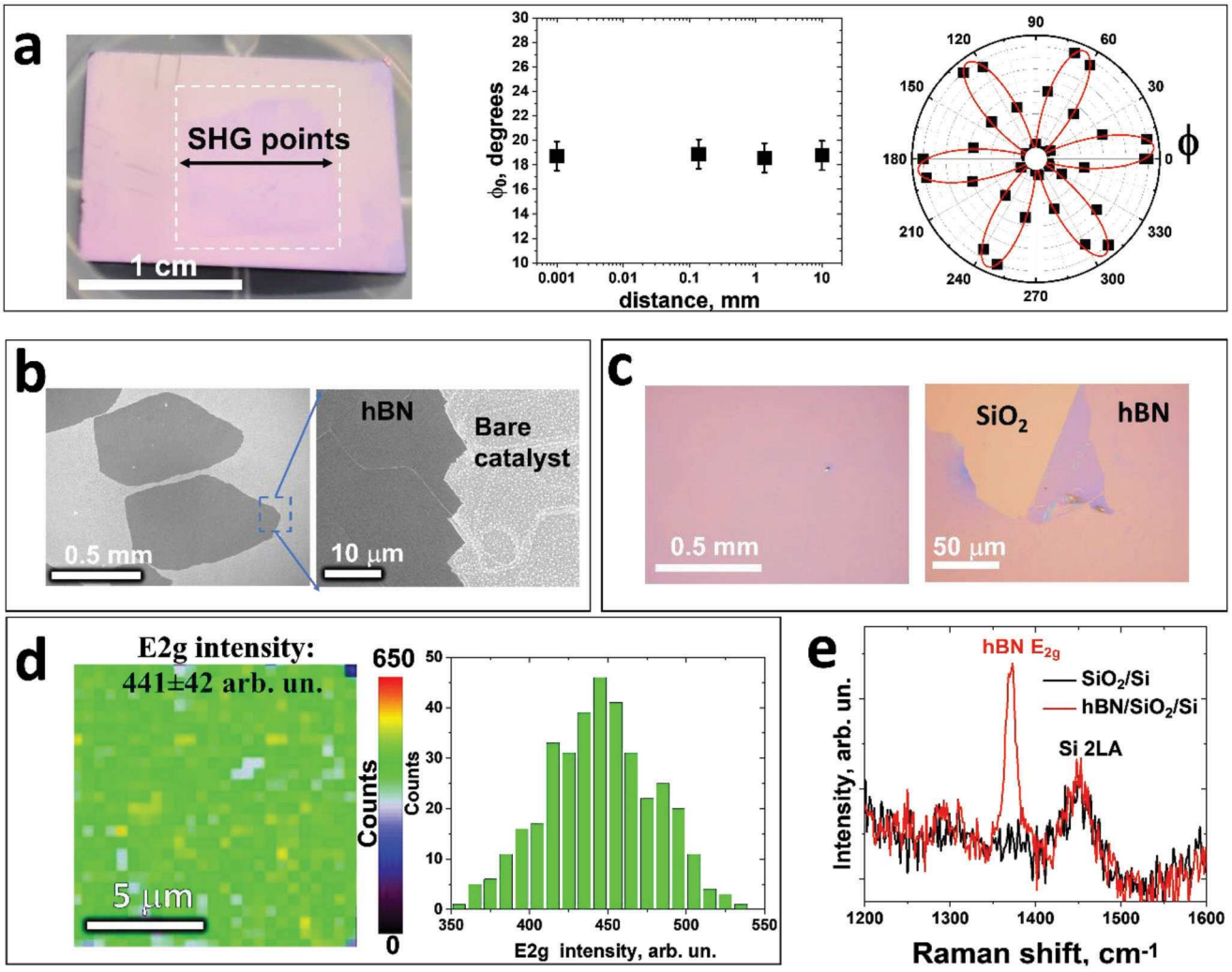

Figure 4. Characterization of hBN grown on FeNi thin films. a) Photograph of the hBN synthesized on Ni/sapphire and transferred onto SiO_2/Si wafer (left). Line profile of hBN crystal orientation and SHG intensity polar plot as a function of excitation polarization angle. 60^0 lobes were obtained at different sample location. b) SEM images of the hBN crystals on the Ni/sapphire catalyst. Identical crystal shapes and orientations are clearly seen (left). Zoomed region onto crystal edge (right). c) Optical images of the hBN grown on 25FeNi and transferred onto SiO_2/Si. d) Raman map intensity of transferred hBN grown on 25FeNi (left). Histograms of the intensity (right). e) Characteristic spectra of hBN/SiO_2/Si (red) and bare SiO_2/Si (black).

substrate using the recently developed evolutionary selection method.[42]

Optical microscope images and Raman mapping in Figure 4c,d suggest good uniformity of the samples. A characteristic Raman spectrum is shown in Figure 4e. Additional E_{2g} Raman intensity, FWHM and band position maps along with their histograms are shown in Figure S10 (Supporting Information). The histograms of the maps illustrate how narrow all the distributions are: intensity – 441 ± 42 arb. un.; FWHM – 17.8 ± 2.0 cm^{-1}, and position 1372.5 ± 0.7 cm^{-1}. These data are obtained for samples grown on 25FeNi chosen to increase the hBN film thickness, as a very weak signal for a monolayer hBN makes it impractical to map over a large area with high resolution. Photoluminescence (PL) analysis of our samples also supports their high-quality, indicating a very low density of optically active defects on a monolayer hBN synthesized from the B/N_2 precursor pair, $<3{\cdot}10^{-4}$ μm^{-2}. For comparison, a monolayer hBN synthesized using ammonia borane on copper substrate[23] has a much greater density of defects, ≈0.6 μm^{-2} (Section 5, Supporting Information).

2.3. Large Scale Synthesis on Industrial Alloys

Nickel and iron are major components of many industrial alloys with extremely large-scale usage. Different means of protecting them for more effective use have always been sought out. For example, covering steel by a protective hBN layer can enhance its performance in many applications, with recent work demonstrating hBN growth on stainless steel under low pressures by employing ammonia borane as precursor.[43] However, that process would be challenging to implement on an industrially relevant scale. In contrast, the cost-effective atmospheric pressure technique presented here uses abundant and benign precursors suitable for convenient industrial scale applications.

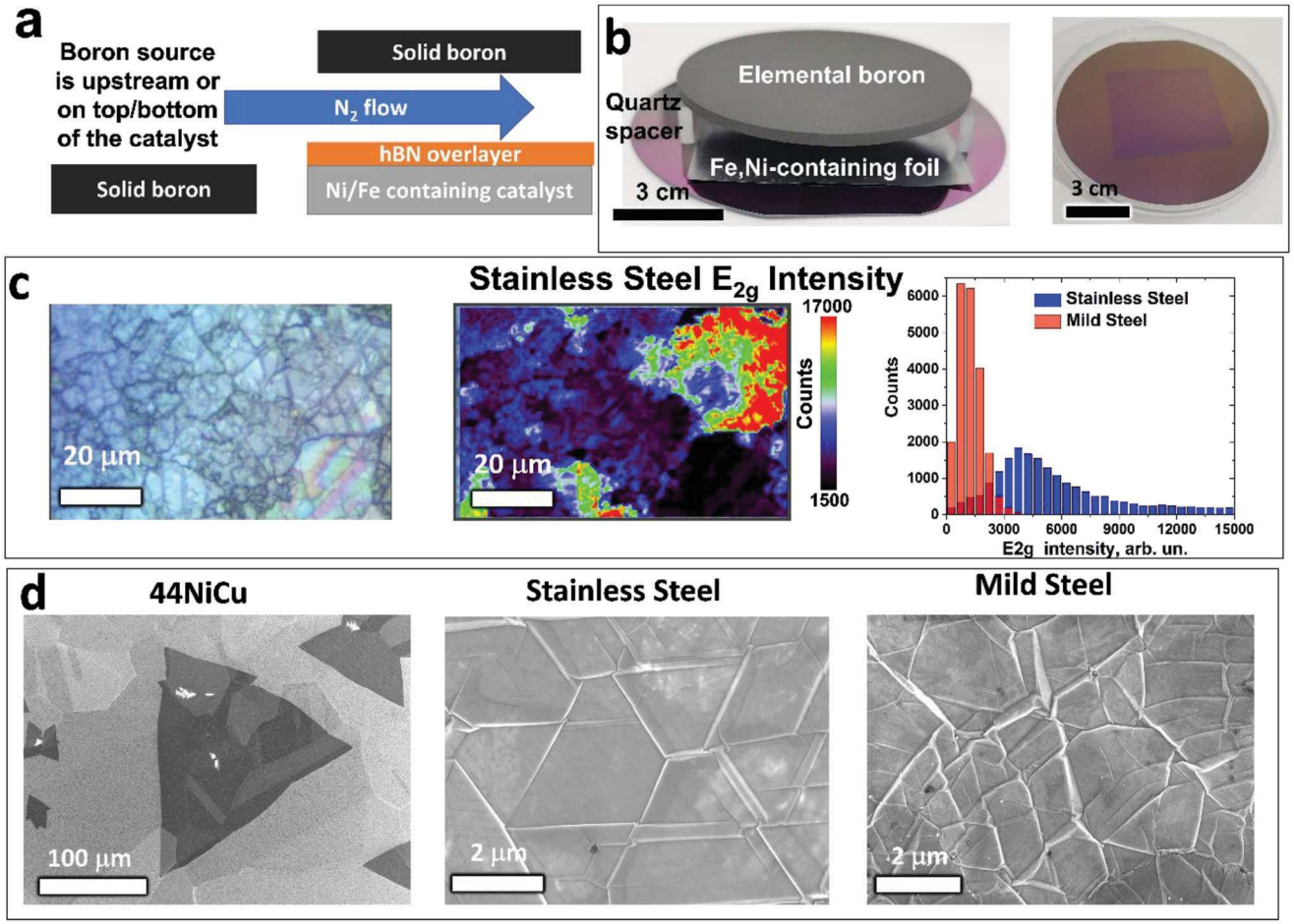

Figure 5. hBN grown on industrial steels and alloys. a) Schematics of the synthesis geometry. The boron piece can be placed upstream or suspended over the catalyst. b) Photograph of the 3″ boron plate suspended over the cupronickel catalyst by the quartz spaces (left). Photo of the hBN synthesized on cupronickel and transferred onto 300 nm SiO_2/Si wafer (right). c) Optical microscope image of hBN grown on stainless steel 304 (left). E_{2g} Raman intensity map of the same region shown (center). Raman map histogram for Stainless steel 304 (blue) and mild steel (red) are shown on the right. d) Comparison of SEM images for hBN grown on cupronickel, where growth was stopped to visualize hBN crystal sizes (44NiCu, left), with stainless steel 304 (center), and mild steel (right).

A typical experiment for covering large parts by hBN is shown in Figure 5a. It sketches the arrangement in a CVD reactor, where a boron source is placed upstream or suspended above the part. In a cold wall reactor, placing the source of boron within a cm range from the catalytic substrate ensures sufficient supply to form hBN, as in the left photo in Figure 5b with a 3″ boron plate suspended over a cupronickel (44NiCu) foil by quartz spacers. In a hot wall geometry, sufficiently large boron pieces can also be placed upstream without pronounced dependence of the growth outcome on a distance from the catalyst. A photo of the synthesized hBN transferred onto 300 nm SiO_2/Si wafer is also given on the right. Raman analysis for that sample is given in Figure S11 (Supporting Information).

An example of hBN grown on stainless steel 304 (SS) is given in Figure 5c along with the Raman maps of the same region. The histogram on the right compares them with the mild steel (MS) substrates. FWHM and band position for E_{2g} are detailed in Figure S12 (Supporting Information). The differences indicate the variation in hBN thicknesses. SS has thicker hBN regions with narrower E_{2g} bands, consistent with the samples grown on thin FeNi thin films. Samples on MS have smaller hBN thickness for the same synthesis conditions: they have blue shifted E_{2g} position compared to SS samples, lower E_{2g} intensities, and larger FWHM. Lower hBN thicknesses on MS are likely due to absence of chromium in the carbon steels. Chromium is known to increase nitrogen solubility, and it is often added in metal fluxes for bulk hBN crystal synthesis.[44–46] Thick hBN samples synthesized at 1550 °C using fluxes are reported to have an E_{2g} band FWHM ≈7.6 cm^{-1}, smaller than the best regions of hBN we observe on SS (≈11 cm^{-1}, Figure S12, Supporting Information).[11] It is due to the thickness difference but may also suggest that the process optimization for CVD can be further improved. Importantly, SHG on the samples grown on steels show well-defined six-lobe signal symmetry suggesting consistent BN layer stacking throughout the whole thickness, as illustrated in Figure S12 (Supporting Information) but cannot rule out formation of rhombohedral boron nitride (rBN) at least on some steel grains.[47] Figure 5d shows SEM images of hBN grown on cupronickel

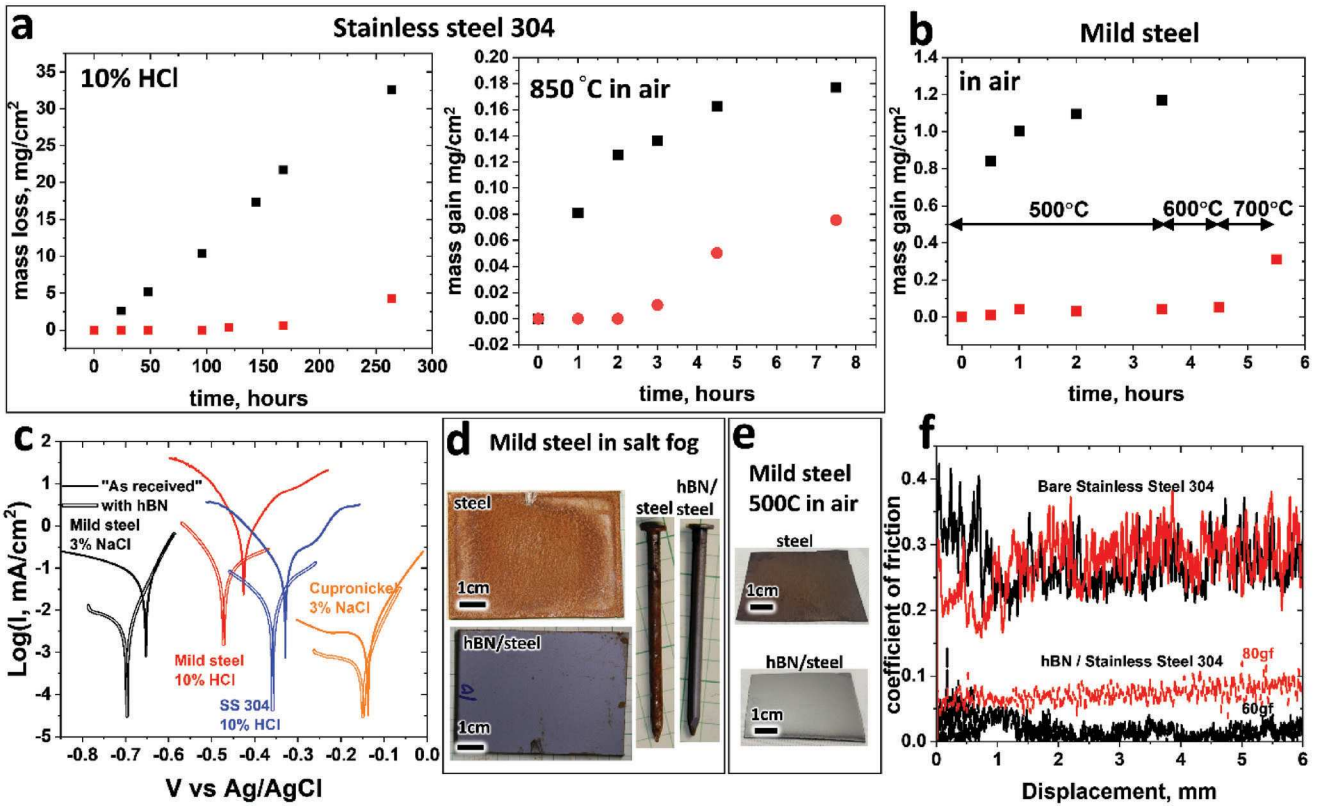

Figure 6. Barrier/tribological properties assessment of hBN grown on industrial steels and alloys. a) Mass loss for as received stainless steel 304 (black) and covered by hBN (red) and mass gain for oxidation in air at 850 °C (right). b) Mild steel (MS) and hBN/MS oxidation in air. c) Tafel plots for steels and cupronickel with/without hBN overlayer in 3% NaCl and 10% HCl solutions. d) Photo of MS and hBN/MS plates and nails after 8 h exposure to salt-fog. e) Photo of MS and hBN/MS after 3.5 h oxidation at 500 °C in air. f) Coefficient of friction for as received stainless steel 304 plate and the same covered by hBN under different loadings – 60 gf (black) and 80 gf (red).

(44NiCu, left), stainless steel 304 (center), and mild steel (right). On 44NiCu, the growth was terminated before the formation of a complete hBN film in order to observe the hBN crystal size, which exceeds 100 µm. Notable is the triangular shape of the hBN crystal despite its extending over multiple metal grains, which supports a possibility of *nonepitaxial* growth regime similar to that on $Ni/SiO_2/Si$ substrate (additional SEM images are shown in Figure S18, Supporting Information). We observe hBN growth on NiCu with 30%, 44%, and 70% of Ni (atomic %) but not for 20% or less. Importantly, hBN on cupronickel has mostly a monolayer appearance, while SS and MS show much thicker films with characteristic multilayer wrinkles and triangular-like morphology supporting precursor dissolution into the substrate and, thus, a precipitation-based growth mechanism, similar to that for thin Fe-rich films (Figures 2 and 3).

Unlike the cupronickels, shorter synthesis time on steels with thickness exceeding 75 µm do not reveal well-defined separated hBN crystals but instead yield thinner hBN layers, still covering the whole substrate surface. Thinner, 25 µm thick stainless steel 304 foils and short synthesis times result in ≈50 µm hBN separated crystals (Figure S13, Supporting Information). Significant dependence on the substrate thickness supports the precipitation-like growth mechanism on steels. Furthermore, the thickness of hBN on steels depends on other synthesis conditions such as the boron source, gas flows, reactor geometry, cooling rates, and temperature. Still, for 1 h synthesis, the hBN coating on MS of 0.75 – 3 mm thickness is typically ≈100 nm thick, as suggested by AFM and optical reflectometry measurements (Figure S7, Supporting Information). The thickness is greater on SS, where it increases to at least ≈300 nm, as judged by the 3 times greater E_{2g} intensity compared to MS, see Figure 5c. Higher intensities for B and N (relative to Fe) are also observed by EDX (Section 7, Supporting Information), supporting the assessment of thicker hBN on SS compared to MS. **Table 1** summarizes the outcomes for hBN synthesis on different substrates.

2.3.1. Synthesis from B_4C and B_2O_3

In addition to elemental boron, other solid boron sources for the growth on steels can be considered. Critical safety and scalability requirements for developing an industry-relevant process narrows down the options. One such potential source, B_2O_3, has appealing higher vapor pressure than elemental B. The growth outcome on mild steel for B_2O_3 placed upstream is similar to that with elemental boron, at least when used along with small amounts of hydrogen, as in our typical case. The comparison of B_2O_3 to B growth outcome is not universal. In the case of stainless steel, usage of B_2O_3 results not only in hBN growth, but also in chromium oxide formation (Figure S20, Supporting

Table 1. Substrates used for hBN growth.

Substrate	Substrate Thickness	hBN domain size	hBN thickness
FeNi thin films on sapphire and SiO_2/Si[a)]	500 nm	Epitaxial growth on Ni/sapphire: cm-sized single hBN crystal (Figure 4)	Depends on Fe content, monolayer for pure nickel, ≈20 layers for 40FeNi. Alloys with Fe at% > 40, results in nonuniform films.
NiCu foils.[b)] Growth starts with Ni at% >20%.	30 µm and 75 µm	Depends on the conditions. For regular experiments, hBN grains exceed 100 µm (Figure 5d)	Mostly monolayer with few-layer islands
Mild steel[c)]	> 100 µm	For mild and stainless steels, precipitation growth mechanism.	Depends on conditions. For 1 h synthesis ≈100 nm
Stainless Steel 304 and 316[c)]	> 100 µm	For thin steel foils, hBN grains exceed 50 µm (Figure S13, Supporting Information)	Depends on conditions. For 1 h synthesis ≈100–300 nm

[a)] Homemade; [b)] 30 µm was purchased from SCHLENK Metal Foils, 75 µm from Stanford materials; [c)] Purchased from McMaster-Carr.

Information). In that case, B_2O_3 can be replaced by B_4C without major differences compared to the elemental boron precursor. Moreover, both elemental boron and boron carbide can be put in contact with stainless steel during growth without noticeable impact on the growth outcome. The latter suggests that boron species transformation does not dictate the growth process outcome and supports the nitrogen-activation being the rate limiting step. Importantly, B_4C is widely used for a well-established steel boriding process[48] to improve wear resistance[49] and corrosion prevention.[50,51] However, we do not observe boride formation on the steel surface under our hBN growth conditions.

2.3.2. Protective and Tribological Properties

As was discussed above, hBN is not only a good dielectric but its film can also serve as a stable protective layer. Figure 6 summarizes these features including protection from corrosion and high-temperature oxidation, along with the tribological properties for hBN films synthesized directly on steels. Figure 6a demonstrates the corrosion protection properties as a reduction of the mass losses in 10% HCl for SS protected by hBN film in comparison to plain stainless 304. The protection lasts for up to 10 days. Longer exposure triggers hBN delamination pointing to the need for more stringent control in lowering the pinhole density and probably additional hBN/steel interface improvement. The latter is likely dependent on the cooling rate. Rare pinholes on such samples can be visualized by conductive AFM (Section 8, Supporting Information). The pinholes can also be seen in the topographic maps and show increased dc current as opposed to the purely capacitive response on the well covered areas. Notably, etching in $FeCl_3$ solution does not reveal obvious pinholes in SEM (Section 8, Supporting Information). Figure 6a also illustrates how the hBN overlayer protects stainless 304 against oxidation in air at 850 °C for several hours. Protection of a mild steel sample against oxidation is less effective, likely due to a lower hBN thickness, as assessed from Raman spectra in Figure 5, and, probably, because of greater pinhole densities. Nevertheless, the improvement compared to unprotected MS is profound: the latter starts to gain mass at 500 °C after 30 min, while hBN protection shifts the stability range to 700 °C (compare Figure 6b,e). Another reason for weaker hBN protection on the industrial MS alloys is likely that they often contain impurities from the manufacturing process, such as Al_2O_3 and MgO particles, which may contribute to the pinhole density increase (Figure S19, Supporting Information). Importantly, unlike for hBN-protected steel, mass gain for plain carbon steel cannot be reliably measured for T > 500 °C (Figure 6e) as it gets severely oxidized with a thick scale that easily flakes off.

Anticorrosion protection is further illustrated by electrochemical measurements. The Tafel plots for different samples in 3% NaCl or 10% HCl solutions are shown in Figure 6c. The corrosion current, I_{corr}, is reduced for all studied steel samples by at least an order of magnitude after hBN protection. A slight cathodic shift of the corrosion potential's, E_{corr}, for hBN protected samples indicates lowering the concentration of oxidative species at the surface and the salt-fog experiments confirm significant corrosion protective properties of the grown hBN. Notably, hBN can be conformally grown on 3D objects such as steel nails and, as illustrated in Figure 6d, their corrosion is visually suppressed by hBN coating.

It is well-known that many 2D materials can reduce the friction coefficient, and some have been used as lubricants for decades.[52] Different mechanisms have been proposed and all relate to the unique 2D structure of hBN. hBN-covered stainless steel has more than an order of magnitude lower coefficient of friction (COF) compared to bare steel, see Figure 6f. Higher loadings during the tribological tests result in the COF increase, likely due to partial punching through the hBN layer by the probe.

3. Conclusions

In summary, we demonstrate a facile and scalable approach for the synthesis of hBN films by atmospheric pressure CVD on top of iron/nickel-containing metallic substrates using solid boron sources (elemental boron, boron oxide, or boron carbide) and molecular nitrogen. For the first time, the hBN coating on stainless steel exhibits improved protection against harsh corrosion over long time and against high-temperature oxidation in air, as well as the lubricating effect comparable to that of Teflon. The reaction mechanism responsible for the hBN growth was thoroughly investigated although the exact boron species transporting through the gas phase could not be unambiguously identified

for elemental boron or carbide feedstocks – boron hydrates or oxide cannot be ruled out. Nitrogen dissociative adsorption on the catalytic substrates was recognized as the rate-limiting step, similar to that in the Haber-Bosch process. This rate-limiting step that happens only at the substrate surface is a key to the process control which allows high quality hBN growth to be scalable and limited only by reactor dimensions. We point out that this approach is not limited by the type of substrates since the most industry-relevant metals (alloys, e.g., steels) are catalytic for this reaction. The iron percentage in the substrate dictates the resulting number of hBN layers, as revealed by investigating various substrates, including pure Ni and FeNi thin films on sapphire on which mono- and few-layer single-crystal hBN is formed, in addition to large samples of industrial stainless, mild steels with flat and complicated 3D shapes. The new growth method using abundant and benign precursors should open new ways for large-scale industrial applications of hBN coating as a versatile protective layer for Ni and Fe-containing alloys, and it can also be adapted to synthesize high-quality single-crystal hBN with controlled layer counts for emerging electronic and photonic devices based on 2D materials.

4. Experimental Section

hBN Growth from Elemental Boron and Molecular Nitrogen: The synthesis was performed in both cold wall and hot wall systems with similar outcomes.

Cold-Wall: The synthesis was performed in 4″ FirstNano EasyTube system. The system was evacuated to 0.1 Torr and filled with the process gas before the synthesis. Regular conditions for the growth were: 1100 °C, 1000 sccm total flow of N_2 + Ar and 25 sccm of H_2. Partial pressures of N_2, H_2, and Ar were controlled by the gas flow ratios keeping atmospheric pressure. Research grade gas purity was used for all experiments. Use of other gases and temperatures were explicitly mentioned in the text. Heating to the targeted temperature was performed in ≈1 min, and the growth was performed for 30 min – 1 h, after which the heating power was turned off, and the sample cooled down to ≈200 °C in ≈5 min. The boron disk was purchased from Kurt Lesker (3″diameter, 0.125″′ thick).

Hot-Wall: A regular Lindberg BlueM 3′′ system was used. The boron piece was suspended over the substrate as in Figure 5a or placed upstream. During heating, 2000 sccm of Ar and 50 sccm of H_2 were flowed until a synthesis temperature is reached (≈25 min). Then, Ar was substituted for N_2 and growth proceeded for the chosen time. After growth, the furnace was opened (fast cool), or controllably cooled with ≈5 C min^{-1} to 800 °C (slow cool). Samples were cooled under the N_2/H_2 flows used for the growth.

hBN Growth from Boron Oxide and Carbides: The growth was performed only in a hot-wall geometry using a 3′′ quartz tube. Samples were suspended over the boron source in an alumina boat or placed downstream. Other growth conditions were similar to those used with elemental boron source. Powders of B_2O_3 (Spectrum Chemical, B1135) and B_4C (Thermo Scientific 04 0504.18) were used as received. The powders were loaded into an alumina boat or homemade stainless steel boat. B_2O_3 melted at ≈450 °C and under our typical growth conditions (≈1000-1200 °C and 0.5–2 L min^{-1} of N_2), B_2O_3 evaporation rates was ≈1.6 mg hr^{-1} cm^{-2}.

Substrates Preparation: *Thin Films*: Ni thin films were deposited on 1 µm SiO_2/Si or 2′′ (0001) Al_2O_3 wafers by e-beam evaporation. Fe films were deposited by sputtering (3 mTorr Ar, 50 W). The thin films were annealed at 1100 °C for 30 min before hBN growth.

Foils: NiCu foils with ≈30 µm thickness were purchased from SCHLENK Metal Foils (30NiCu, 44NiCu, 70NiCu, and 100Ni, corresponding to 30%, 44%, 70%, and 100% Ni). NiCu foils with 10, 15, 20, and 30% Ni having 75 µm thickness were purchased from Stanford Advanced Materials (Irvine, CA). Iron foils were purchased from Alfa Aesar (0.1 mm thick) and Stanford Materials, Irvine, CA (0.05 mm thick). Stainless steel and mild steel foils, sheets and nails, and Inconel 625 sheets were purchased from McMaster-Carr. The steel parts were cleaned with acetone, isopropanol, rinsed in DI water, and dried with an air gun.

hBN Transfer: *Thin films/NiCu foils*: PMMA was spin-coated on a sample with grown hBN (495 A4 Microchem, 2000 rpm, 45 s) and baked for 2 min on a hot plate at 180 °C. The catalyst was dissolved using regular Transene copper etchant and the released sample was thoroughly washed in DI water baths before being transferred onto a ≈300 nm SiO_2/Si wafer. PMMA was subsequently removed by acetone.

Steels: hBN was thick enough to sustain the transfer process without a PMMA supporting layer. Steel etching, hBN washing was identical to the hBN grown on thin films/NiCu, but omitting the PMMA casting step.

XRD: X-ray diffraction (XRD) measurements at Cu Kα wavelength (1.5418 Å) were conducted in a 2*q*-*q* mode using a PANalytical X'Pert Pro MPD equipped with an X'Celerator solid-state detector.

XPS: XPS was acquired using Thermo Scientific Model K-Alpha XPS instrument. The spectra were obtained using micro-focused, monochromatic Al Kα X-rays (1486.6 eV) with 400 µm X-ray spot size. Details were in Supporting Information.

Raman and Photoluminescence: The photoluminescence (PL) and Raman maps were obtained by two different setups with similar outcomes. The first setup was based on the InVia Qontor (Renishaw) commercially available system. The excitation with a 532 nm laser was delivered through a 100x (NA = 0.85) or 20x (NA = 0.4) Leica lens, and the power on the sample was 2.4 and 12.14 mW, respectively. The scattered signal was collected by the same objective and passed through a set of ultra-narrow Notch filters onto 1800 and 300 lines mm^{-1} gratings for Raman and photoluminescence measurements, respectively. The mapping measurements were conducted with 0.5 µm steps size (Figure 4d) and 1 µm (Figure 5c).

The second setup was a custom-built micro-PL system. The PL was excited with a 532 nm laser (Excelsior, Spectra Physics, 100 mW) through an upright microscope using a 100x-objective (NA = 0.9). The PL light was analyzed by a spectrometer (Spectra Pro 2300i, Acton, f = 0.3 m) that was coupled to the microscope and equipped with 150, 600, and 1800 lines mm^{-1} gratings and a CCD camera (Pixis 256BR, Princeton Instruments). The mapping measurements were conducted with 0.2 µm steps size (Supporting Information).

Second Harmonic Generation: Second harmonic generation (SHG) measurements were conducted using a 40 fs Ti:Sapphire laser (Micra, Coherent) at 800 nm and 80 MHz repetition rate. The laser beam was passed through a half-wave plate mounted in a rotation stage and was directed into an upright microscope (Olympus) and focused onto a sample surface using a 100 x microscope objective (Numerical Aperture: NA = 0.9) to a ≈1.5 µm spot. The laser energy at the sample surface was ≈1 mW. The SHG light was collected in backscattering configuration using the same objective and was directed into a monochromator (Spectra Pro 2300i, Acton, f = 0.3 m) that was coupled to the microscope and equipped with a 150 grooves mm^{-1} grating and a CCD camera (Pixis 256BR, Princeton Instruments). Before entering the monochromator, the SHG light passed through a short-pass cut-off filter (650 nm) to filter out the fundamental excitation light at 800 nm and a polarizer to select SHG polarization colinear or cross relative to the polarization of the excitation light.

Atomic Force Microscopy: Atomic force microscopy (AFM) was performed on two instruments with similar outcomes. Cypher AFM (Asylum research and Oxford Instruments) using AC mode with a commercially available Multi75E-G (BudgetSensors) made of silicon, with a Chromium/Platinum conductive coating, a nominal spring constant of 3 N m^{-1} and a resonance frequency of 75 kHz. Bruker Dimension Icon AFM in the tapping mode with an Si probe (TESPA-V2, 7 nm tip radius, 37 N m^{-1} spring constant.)

Coefficient of Friction: The UMT Tribolab (Bruker) was used to obtain the coefficient of friction data. The load block used in this test was DFM-2.0 with a brale tip indenter. Scanning speed was 0.1 mm s^{-1} with either 60 or 80 gf applied force.

Corrosion: Corrosion data was obtained using Biologic SP-300 potentiostat and a basic BMM EC cell from Redoxme AB with 0.2 cm^2 active area. Mass gain/reduction was obtained using regular balance after soaking in the solution of interest or heating up in the tube furnace under the air for different periods of time. Samples sizes for the latter were at least 5 cm^2.

Salt-Fog: Salt fog experiments were performed in an Auto Technology salt fog corrosion chamber according to ASTM standard B117-19. The fog consisted of a 5% NaCl solution that was sprayed at a temperature of 35 °C.

STEM: Atomic resolution high-angle annular dark field (HAADF) scanning transmission electron microscope (STEM) images of single layer hBN were acquired using a Nion UltraSTEM 200 operated with an accelerating voltage of 80 kV. The sample was heated in situ to 1200 °C to clean off surface contaminants[53] and then imaged at room temperature.

Supporting Information

Supporting Information is available from the Wiley Online Library or from the author.

Acknowledgements

This work was supported by the Center for Nanophase Materials Sciences (CNMS), which is a US Department of Energy, Office of Science User Facility at Oak Ridge National Laboratory (ORNL). Support for I.V. was partially provided through Strategic Hire funding through the Laboratory Directed Research and Development Program of ORNL. Support for P.R.K. and P.C. was partially provided through NSF CAREER award #1944134 and DOE Early Career Research Program award #DE-SC0022915. P.D.R. and R.E. acknowledge The University of Tennessee Materials Research Science & Engineering Center - The Center for Advanced Materials and Manufacturing - is supported by the National Science Foundation under DMR No. 2309083.

Conflict of Interest

The authors declare no conflict of interest.

Data Availability Statement

The data that support the findings of this study are available in the supplementary material of this article.

Keywords

2D materials, anticorrosion, CVD, hBN, oxidation protection, single crystals, steel

Received: August 22, 2023
Revised: September 27, 2023
Published online: October 20, 2023

[1] M. J. Molaei, M. Younas, M. Rezakazemi, *Acs Appl. Electron Ma* **2021**, *3*, 5165.
[2] K. Zhang, Y. Feng, F. Wang, Z. Yang, J. Wang, *J. Mater. Chem. C* **2017**, *5*, 11992.
[3] S. Roy, X. Zhang, A. B. Puthirath, A. Meiyazhagan, S. Bhattacharyya, M. M. Rahman, G. Babu, S. Susarla, S. K. Saju, M. K. Tran, *Adv. Mater.* **2021**, *33*, 2101589.
[4] A. E. Naclerio, P. R. Kidambi, *Adv. Mater.* **2023**, *35*, 2207374.
[5] G. Chilkoor, S. P. Karanam, S. Star, N. Shrestha, R. K. Sani, V. K. K. Upadhyayula, D. Ghoshal, N. A. Koratkar, M. Meyyappan, V. H. B. N. Gadhamshetty, *Acs Nano* **2018**, *12*, 2242.
[6] F. Mahvash, S. Eissa, T. Bordjiba, A. C. Tavares, T. Szkopek, M. Siaj, *Sci. Rep.* **2017**, *7*, 42139.
[7] G. Chilkoor, K. Jawaharraj, B. Vemuri, A. Kutana, M. Tripathi, D. Kota, T. Arif, T. Filleter, A. B. Dalton, B. I. Yakobson, M. Meyyappan, M. M. Rahman, P. M. Ajayan, V. Gadhamshetty, *ACS Nano* **2020**, *14*, 14809.
[8] Z. Liu, Y. J. Gong, W. Zhou, L. L. Ma, J. J. Yu, J. C. Idrobo, J. Jung, A. H. MacDonald, R. Vajtai, J. Lou, *Nat. Commun.* **2013**, *4*, 2541.
[9] X. Tang, H. Wang, C. Liu, X. Zhu, W. Gao, H. Yin, *ACS Appl. Nano Mater.* **2021**, *4*, 12024.
[10] T. Taniguchi, K. Watanabe, *J. Cryst. Growth* **2007**, *303*, 525.
[11] J. H. Li, J. Y. Wang, X. T. Zhang, C. Elias, G. H. Ye, D. Evans, G. Eda, J. M. Redwing, G. Cassabois, B. Gil, *Acs Nano* **2021**, *15*, 7032.
[12] Y. Li, X. Wen, C. Tan, N. Li, R. Li, X. Huang, H. Tian, Z. Yao, P. Liao, S. Yu, S. Liu, Z. Li, J. Guo, Y. Huang, P. Gao, L. Wang, S. Bai, L. Liu, *Nanoscale* **2021**, *13*, 11223.
[13] C. Maestre, B. Toury, P. Steyer, V. Garnier, C. Journet, *J. Phys. Mater.* **2021**, *4*, 044018.
[14] Z. Y. Shi, X. J. Wang, Q. T. Li, P. Yang, G. Y. Lu, R. Jiang, H. S. Wang, C. Zhang, C. X. Cong, Z. Liu, *Nat. Commun.* **2020**, *11*, 849.
[15] Y. Uchida, S. Nakandakari, K. Kawahara, S. Yamasaki, M. Mitsuhara, H. Ago, *ACS Nano* **2018**, *12*, 6236.
[16] M. H. Khan, H. K. Liu, X. Sun, Y. Yamauchi, Y. Bando, D. Golberg, Z. Huang, *Mater. Today* **2017**, *20*, 611.
[17] K.i K. Kim, H. S. Lee, Y. H. Lee, *Chem. Soc. Rev.* **2018**, *47*, 6342.
[18] J. S. Lee, S. H.o Choi, S. J. Yun, Y. I.n Kim, S. Boandoh, J.i-H. Park, B. G. Shin, H. Ko, S. H. Lee, Y.-M. Kim, Y. H. Lee, K.i K. Kim, S. M. Kim, *Science* **2018**, *362*, 817.
[19] L.i Wang, X. Xu, L. Zhang, R. Qiao, M. Wu, Z. Wang, S. Zhang, J. Liang, Z. Zhang, Z. Zhang, W. Chen, X. Xie, J. Zong, Y. Shan, Y.i Guo, M. Willinger, H. Wu, Q. Li, W. Wang, P. Gao, S. Wu, Y.i Zhang, Y. Jiang, D. Yu, E. Wang, X. Bai, Z.-J. Wang, F. Ding, K. Liu, *Nature* **2019**, *570*, 91.
[20] T. A. Chen, C. P. Chuu, C. C. Tseng, C. K. Wen, H. S. P. Wong, S. Y. Pan, R. T. Li, T. A. Chao, W. C. Chueh, Y. F. Zhang, *Nature* **2020**, *579*, 219.
[21] S. Fukamachi, P. Solís-Fernández, K. Kawahara, D. Tanaka, T. Otake, Y.-C. Lin, K. Suenaga, H. Ago, *Nat. Electron.* **2023**, *6*, 126.
[22] K. Y. Ma, L. Zhang, S. Jin, Y. Wang, S. I.n Yoon, H. Hwang, J. Oh, D.a S. Jeong, M. Wang, S. Chatterjee, G. Kim, A.-R. Jang, J. Yang, S. Ryu, H.u Y. Jeong, R. S. Ruoff, M. Chhowalla, F. Ding, H. S. Shin, *Nature* **2022**, *606*, 88.
[23] Y. Stehle, H. M. Meyer, R. R. Unocic, M. Kidder, G. Polizos, P. G. Datskos, R. Jackson, S. N. Smirnov, I. V. Vlassiouk, *Chem. Mater.* **2015**, *27*, 8041.
[24] J.i-H. Park, A.-Y.u Lu, M. M. Tavakoli, N.a Y. Kim, M.-H. Chiu, H. Liu, T. Zhang, Z. Wang, J. Wang, L. G. P. Martins, Z. Luo, M. Chi, J. Miao, J. Kong, *Nano Lett.* **2023**, *23*, 4741.
[25] A. Bansal, X. Zhang, J. M. Redwing, *J. Mater. Res.* **2021**, *36*, 4678.
[26] C. Gómez-Aleixandre, A. Essafti, M. Fernández, J. L. G. Fierro, J. M. Albella, *J. Phys. Chem.-US* **1996**, *100*, 2148.
[27] H. Yamada, S. Inotsume, N. Kumagai, T. Yamada, M. Shimizu, *Phys. Status Solidi A* **2021**, *218*, 2000241.
[28] H. Yamada, S. Inotsume, N. Kumagai, T. Yamada, M. Shimizu, *Phys. Status Solidi B* **2020**, *257*, 1900318.
[29] T. Kandemir, M. E. Schuster, A. Senyshyn, M. Behrens, R. Schlögl, *Angew. Chem. Int. Edit.* **2013**, *52*, 12723.

[30] J. Humphreys, R. Lan, S. W. Tao, *Adv. Energ. Sust. Res.* **2021**, *2*, 2000043.
[31] C. Kowanda, M. O. Speidel, *Scripta. Mater.* **2003**, *48*, 1073.
[32] K. I. Portnoi, V. M. Romashov, V. M. Chubarov, M. K.h. Levinskaya, S. E. Salibekov, *Powder Met. Met. Ceram.* **1967**, *6*, 99.
[33] T. B. Cameron, J. E. Morral, *Metall. Trans. A* **1986**, *17*, 1481.
[34] M. J. Matthews, M. A. Pimenta, G. Dresselhaus, M. S. Dresselhaus, M. Endo, *Phys. Rev. B* **1999**, *59*, R6585.
[35] A. C. Ferrari, *Solid State Commun.* **2007**, *143*, 47.
[36] L. G. Cancado, K. Takai, T. Enoki, M. Endo, Y. A. Kim, H. Mizusaki, A. Jorio, L. N. Coelho, R. Magalhaes-Paniago, M. A. Pimenta, *Appl. Phys. Lett.* **2006**, *88*, 163106.
[37] C. Oshima, A. Nagashima, *J. Phys.-Condens. Mat.* **1997**, *9*, 1.
[38] J. Dong, L. Zhang, X. Dai, F. Ding, *Nat. Commun.* **2020**, *11*, 5862.
[39] A. A. Tonkikh, E. N. Voloshina, P. Werner, H. Blumtritt, B. Senkovskiy, G. Guntherodt, S. S. P. Parkin, Y. S. Dedkov, *Sci. Rep.* **2016**, *6*, 23547.
[40] Y. Hu, J. Peng, M. Pan, W. Qiu, R. Wu, J. Hu, N. Hu, F. Cheng, R. Huang, F. Li, D. Chen, Q.i Zhang, P. Li, *J. Mater. Sci.* **2021**, *56*, 3220.
[41] L. M. Malard, T. V. Alencar, A. P. M. Barboza, K. F. Mak, A. M. De Paula, *Phys. Rev. B* **2013**, *87*, 201401.
[42] I. V. Vlassiouk, Y. Stehle, P. R. Pudasaini, R. R. Unocic, P. D. Rack, A. P. Baddorf, I. N. Ivanov, N. V. Lavrik, F. List, N. Gupta, K. V. Bets, B. I. Yakobson, S. N. Smirnov, *Nat. Mater.* **2018**, *17*, 318.
[43] S. Jia, W. Chen, J. Zhang, C. Y. Lin, H. Guo, G. Lu, K. Li, T. Zhai, Q. Ai, J. Lou, *Mater Today Nano* **2021**, *16*, 100135.
[44] Y. Kubota, K. Watanabe, O. Tsuda, T. Taniguchi, *Chem. Mater.* **2008**, *20*, 1661.
[45] T. B. Hoffman, B. Clubine, Y. Zhang, K. Snow, J. H. Edgar, *J. Cryst. Growth* **2014**, *393*, 114.
[46] S. Liu, R. He, Z. Ye, X. Du, J. Lin, H. Jiang, B. Liu, J. H. Edgar, *Cryst. Growth Des.* **2017**, *17*, 4932.
[47] J. Qi, C. Ma, Q. Guo, C. Ma, Z. Zhang, F. Liu, X. Shi, L. Wang, M. Xue, M. Wu, P. Gao, H. Hong, X. Wang, E. Wang, C. Liu, K. Liu, *Adv. Mat.* **2023**, https://doi.org/10.1002/adma.202303122.
[48] R. A. García-León, J. Martínez-Trinidad, I. Campos-Silva, *T Indian I Metals* **2021**, *74*, 541.
[49] E. Mertgenc, O. F. Kesici, Y. Kayali, *Mater. Res. Express* **2019**, *6*, 076420.
[50] H. Tavakoli, S. M. Mousavi Khoie, *Mater. Chem. Phys.* **2010**, *124*, 1134.
[51] A. Günen, M. Serdar Karakas, B. Kurt, A. Çalik, *Anti-Corros Method M* **2014**, *61*, 112.
[52] L. C. Liu, M. Zhou, L. Jin, L. C. Li, Y. T. Mo, G. S. Su, X. Li, H. W. Zhu, Y. Tian, *Friction* **2019**, *7*, 199.
[53] O. Dyck, S. Kim, S. V. Kalinin, S. Jesse, *J. Vac. Sci. Technol. B* **2018**, *36*, 011801.